Langmuir

Article

pubs.acs.org/Langmuir

Air-Stable Spin-Coated Naphthalocyanine Transistors for Enhanced Chemical Vapor Detection

James E. Royer, Chengyi Zhang, Andrew C. Kummel,* and William C. Trogler*

Department of Chemistry and Biochemistry, University of California, San Diego, La Jolla, California 92093, United States

Ⓢ *Supporting Information*

ABSTRACT: Air-stable organic thin-film transistor (OTFT) sensors fabricated using spin-cast films of 5,9,14,18,23,27,32,36-octabutoxy-2,3-naphthalocyanine (OBNc) demonstrated improved chemical vapor sensitivity and selectivity relative to vacuum-deposited phthalocyanine (H_2Pc) OTFTs. UV−vis spectroscopy data show that annealed spin-cast OBNc films exhibit a red-shift in the OBNc Q-band λ_{max} which is generally diagnostic of improved π-orbital overlap in phthalocyanine ring systems. Annealed OBNc OTFTs have mobilities of 0.06 $cm^2\ V^{-1}\ s^{-1}$, low threshold voltages ($|V_{th}| < 1$ V), and on/off ratios greater than 10^6. These air-stable device parameters are utilized for sensing modalities which enhance the sensitivity and selectivity of OBNc OTFTs relative to H_2Pc OTFTs. While both sensors exhibit mobility decreases for all analytes, only OBNc OTFTs exhibit V_{th} changes for highly polar/nonpolar analytes. The observed mobility decreases for both sensors are consistent with electron donation trends via hydrogen bonding by basic analytes. In contrast, V_{th} changes for OBNc sensors appear to correlate with the analyte's octanol−water partition coefficient, consistent with polar molecules stabilizing charge in the organic semiconductor film. The analyte induced V_{th} changes for OBNc OTFTs can be employed to develop selective multiparameter sensors which can sense analyte stabilized fixed charge in the film.

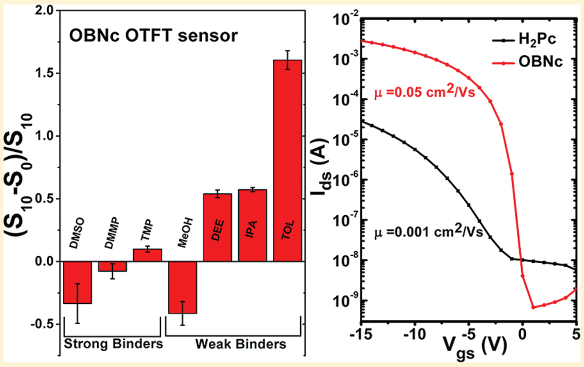

INTRODUCTION

Solution processable organic semiconductors are desirable for large-area sensor applications due to the multifunctional material and device characteristics.[1−3] Organic thin-film transistors (OTFTs) are strong candidates for chemical sensors due to the presence of multiple chemically responsive device parameters such as drain-current (I_{ds}), field-effect mobility (μ_{FE}), and threshold voltage (V_{th}).[4,5] The sensor response can also be tuned by functionalizing the organic film or insulator interface with additional receptors.[6−8] Sensors that can be processed using solution-based approaches are desirable for large-area applications such as array patterning for low-cost electronic noses.[9,10] Numerous vacuum-deposited metal−phthalocyanines (MPcs) have been used for selective OTFT sensors, but these unsubstituted MPcs are not compatible with solution-deposition techniques.[11] Additionally, MPcs typically exhibit low field-effect mobility which prevents effective analysis of the OTFT sensor parameters. Therefore, obtaining solution-processable substituted MPc OTFTs with improved performance could yield new synthetic pathways for selective chemical sensing.

MPc materials are not compatible with solution deposition methods due to the poor solubility of MPcs in organic solvents.[12] The solubility can be improved by adding peripheral or nonperipheral substituents to the phthalocyanine ring.[13] Metal−naphthalocyanines (MNcs) are structurally similar to MPcs but have additional fused benzene rings on the periphery, which extend the π-conjugated system. MNcs exhibit excellent thermal stability and a reduced optical band gap and can be functionalized with peripheral or nonperipheral substituents for use in solution-processed thin films.[14,15]

While the outer ring substitutions can improve MPc solubility, MPc sensor response is primarily determined by the center metal atom, which acts as a preferential binding site.[16,17] In metal-free phthalocyanine (H_2Pc), the inner N−H groups act as preferential hydrogen bond receptors for basic analytes.[18] A similar observation was recently reported for spin-coated metal-free porphyrin OTFTs.[19] The phthalocyanine and porphyrin sensor response to specific analytes is attributed to specific intermolecular binding as opposed to grain boundary adsorption density.

MPc and metalloporphyrin OTFTs are limited in practical applications due to long-term device instability when operated in ambient air.[20,21] The device instability is attributed to ambient oxidants or humidity which cause mobility decreases, threshold voltage shifts, and/or lower I_{on}/I_{off} ratios.[22] Air-stable organic semiconductor films are essential for chemical sensing to prevent cross-sensitivity to ambient interferents and ambient induced drift.

Received: November 14, 2011
Revised: February 9, 2012
Published: February 29, 2012

In the present work, air-stable OTFT sensors were fabricated using spin-cast films of 5,9,14,18,23,27,32,36-octabutoxy-2,3-naphthalocyanine (OBNc). Synthesis of OBNc and OBMNc compounds follows a metal template synthetic approach using naphthalonitrile precursors, which is similar to phthalocyanine synthetic methods and readily adaptable to commercial scale up. Spectroscopic data reveal a high degree of intermolecular order for solution-processed OBNc films, which is attributed to the butoxy substituents providing a stable crystal structure. Spin-cast OBNc OTFTs on octadecyltrichlorosilane (OTS) treated SiO_2 substrates exhibit field-effect mobilities of 0.06 cm^2 V^{-1} s^{-1}, $|V_{th}| < 1$ V, and I_{on}/I_{off} ratios greater than 10^6. These values are comparable to most solution-processed MPc/MNc OTFTs[23,24] and better than vacuum-deposited H_2Pc OTFTs.[12,19] These enhancements to OTFT performance improve the sensitivity and selectivity for OBNc OTFT sensors relative to vacuum-deposited H_2Pc OTFT sensors. The improved mobility and I_{on}/I_{off} ratio enables enhanced selectivity via analyte induced V_{th} shifts while monitoring I_{ds} in the OBNc OTFT subthreshold regime ($V_{gs} \approx V_{th}$). Analyte stabilized charge causes V_{th} shifts exclusively for OBNc OTFTs, yielding large irreversible $\Delta I_{ds}/I_{ds0}$ response. H_2Pc OTFTs do not exhibit improved sensor response, and therefore are not selective, when monitored at $V_{gs} \approx V_{th}$ due to the lower mobility and I_{on}/I_{off} ratio. When sensing within the accumulation regime ($V_{gs} < V_{th}$), the sensitivity for OBNc sensors is improved by 2−5 times the H_2Pc sensitivity. The improved sensitivity for OBNc suggests that the analytes more strongly perturb the OBNc electronic states, which is evidenced by larger mobility decreases for OBNc sensors. The convenient synthetic approach for fabricating OBNc OTFTs combined with their air stability and sensor performance makes OBNc a promising candidate for OTFT sensors.

EXPERIMENTAL METHODS

OBNc Synthesis. 5,9,14,18,23,27,32,36-Octabutoxy-2,3-naphthalocyanine (OBNc) was synthesized by modified literature methods.[25] Under an inert argon atmosphere, 1-butanol (5 mL) was added into a two-neck round-bottom flask with freshly cut lithium wire (250 mg), and the mixture was refluxed for 20 min and then cooled. 1,4-Dibutoxy-2,3-dicyanonaphthalene (1.00 g) was added, and the resulting mixture refluxed for 1 h and then cooled. The suspension formed was diluted with glacial acetic acid (10 mL), and the acidified suspension was stirred for 4 h and evaporated to dryness with a rotary evaporator. The residue was dissolved in dichloromethane, and the solution was washed with hydrochloric acid (10%) and water. The solution was evaporated over dried ($MgSO_4$). The residue was purified by column chromatography using an alumina column (Al_2O_3, III, toluene) and polymer gel column (Biobeads S-X1, toluene). Finally, the product was recrystallized from chloroform−methanol and vacuum-dried (50 °C) for 12 h (673 mg, 67%). NMR (400 MHz, C_6D_6): δ 9.24 (*m*, 8H), 7.68 (*m*, 8H), 5.40 (*t*, 16H), 2.38 (*m*, 16H), 2.25 (*s*, 2H), 1.68 (*m*, 16H), 1.02 (*m*, 24H). MS (ESI-MS) for $[M + H]^+$ with M as $C_{80}H_{90}N_8O_8$: calcd, *m/z*, 1291.69; found, *m/z*, 1291.65. Elemental analysis for $C_{80}H_{90}N_8O_8$, calcd: %C 74.39, %H 7.02, %N 8.68; found: %C 74.40, %H 7.28, %N 8.71.

Device Fabrication and Characterization. Bottom-gate, bottom-contact thin-film transistor substrates were fabricated on thermally grown SiO_2/n^+Si substrates (Silicon Quest). A bilayer resist lift-off process was used for electrode patterning to minimize the contact resistance.[26] Electrodes composed of a 5 nm Ti adhesion layer and 45 nm Au were deposited by electron-beam deposition under high vacuum. The 100 nm SiO_2 layer ($C_i = 3.45 \times 10^{-8}$ F cm^{-2}) functioned as the gate oxide and the n^+Si as the gate electrode, which was contacted by wet-etching through the SiO_2 and an additional Ti/Au deposition. The OTFT substrates were treated with octadecyltrichlorosilane (OTS) by immersion in a 1.25 mM OTS solution in toluene. OBNc thin films were spin-cast from a 2 wt % OBNc solution in toluene. The films had a thickness of ~50 nm as determined by profilometry. H_2Pc OTFTs were fabricated on OTS-treated substrates using commercial H_2Pc (Aldrich), which was purified by multiple-zone sublimation. The H_2Pc was deposited at a rate of 1 Å s^{-1} under ultrahigh vacuum onto substrates held at room temperature.

UV−vis measurements were performed under ambient conditions using a Perkin-Elmer Lambda 35 UV−vis spectrometer. Atomic force microscopy (AFM) measurements were performed with a Nanoscope IV scanning probe microscope in tapping mode using a Nanosensors SSS-NCHR-20 ultrasharp Si probe.

Current−voltage measurements were recorded using an Agilent B1500 semiconductor parameter analyzer. All measurements were recorded in the dark, under ambient air, and at room temperature. The OBNc chips were stored in the dark in ambient conditions to test the device stability. The field-effect mobility and threshold voltage were calculated based on the equation for OTFT saturation mode operation, $I_{ds} = (WC_i/2L)\mu_{FE}(V_{gs} - V_{th})^2$, where C_i is the gate oxide capacitance, μ_{FE} is the field-effect mobility, V_{th} is the threshold voltage, W is the channel width, and L is the channel length.

Sensor Testing. Measurements during chemical sensing were recorded on a National Instruments PXI-6259 M-Series Multifunction DAQ and controlled by a custom-designed LabVIEW program. The devices were mounted onto a ceramic DIP, and drain-current measurements were calculated by recording the voltage drop across a resistor. OTFT transfer curves (I_{ds}−V_{gs}) were recorded every 30 s by a gate voltage (V_{gs}) sweep from +10 to −10 V in 2 V steps at 10 V s^{-1} with the drain voltage (V_{ds}) held at −10 V. Transient μ_{FE} was calculated from the linear section of the transfer curves. Analyte pulses were introduced to a stainless steel flow chamber held at 25 °C using the methods previously reported from this lab.[18,19] All doses were for a 5 min duration followed by a 1 h recovery. The carrier and purge gas was clean dry air (Praxair, <2 ppm H_2O, <0.02 ppm NO_x).

RESULTS AND DISCUSSION

Single Crystal XRD and UV−vis Characterization. The synthesized OBNc was purified using a series of alumina and polymer gel columns and then recrystallized from a chloroform−methanol solution. A high degree of purity for OBNc was revealed by both spectroscopic and elemental analysis. OBNc is soluble in a range of organic solvents, such as chloroform, toluene, and tetrahydrofuran. To determine the solid-state structure, single crystals of OBNc were grown by slow evaporation from a toluene solution. X-ray structure analyses of the single crystals indicated that the individual units of the macrocycle, i.e., a pyrrole ring or naphthyl ring, were almost planar. The dihedral angles between an individual pyrrole ring and its associated naphthyl ring were less than 5°. The angles between planes of adjacent naphthyl rings were about 12°. The molecular arrangement viewed parallel to the *c* and *a* axes are shown in Figure 1. The molecules are arranged in offset stacks with the butoxy side chains acting as spacers between each molecule. The shortest distance between planes of naphthalocyanine molecules within a stack is ca. 6.6 Å, and the distance between the centers of the molecules is 8.0 Å. UV−vis spectra for OBNc spin-cast films have a red-shifted Q-band λ_{max} (887 nm) relative to the Q-band λ_{max} for OBNc in toluene solution (864 nm) (Figure 2). Annealing the OBNc film at 120 °C for 1 min increased the Q-band red-shift to 918 nm. As reported in the literature, the red-shift value correlates with the center-to-center distance of adjacent parallel naphthalocyanines. Larger red-shifts correlate with a decrease in the center-to-center distance in a J-aggregate type structure.[27,28] Therefore, the increased red-shift observed after annealing is consistent with the improved transport properties

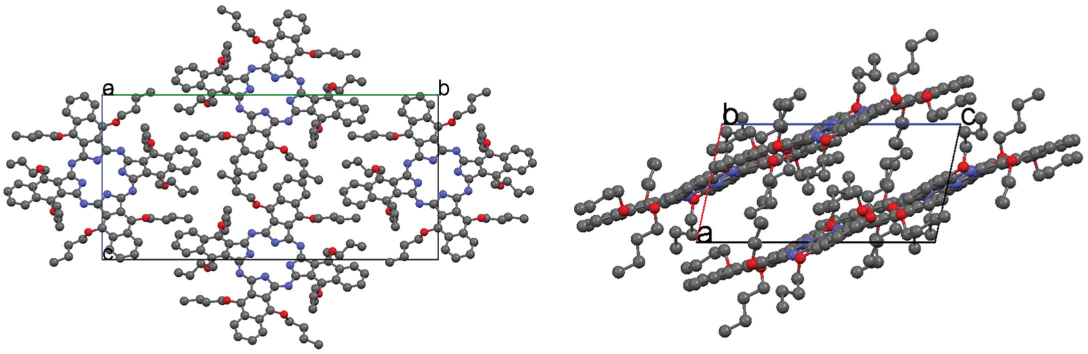

Figure 1. Crystal structure of 5,9,14,18,23,27,32,36-octabutoxy-2,3-naphthalocyanine (OBNc). (Hydrogen atoms and toluene solvate molecules were removed for clarity.) The shortest distance between planes of naphthalocyanine molecules within a stack is ca. 6.6 Å, and the distance between the centers of the molecules is 8.0 Å. Oxygen atoms are shown in red, and nitrogen atoms are shown in blue.

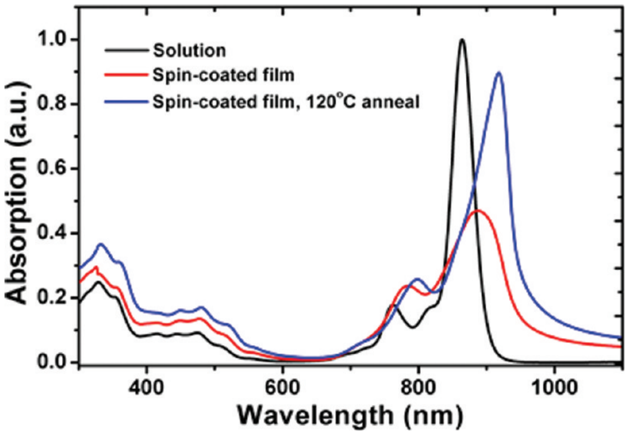

Figure 2. UV−vis absorption spectra of OBNc in solution and thin films. A red-shift of the Q-band $\lambda_{\max}$ is observed for the spin-cast film on glass substrates (887 nm) relative to the solution (864 nm). Annealing the spin-cast film at 120 °C for 1 min increased the Q-band red-shift to a $\lambda_{\max}$ of 918 nm, consistent with increased π overlap in the OBNc J-aggregate structure.

due to enhanced $\pi-\pi$ overlap between adjacent OBNc molecules in a J-aggregate structure. Even though the interplanar spacing of OBNc exceeds that in vacuum-deposited H_2Pc, the field-effect mobilities obtained are superior for the naphthalocyanines. This may arise from the extended conjugation of the naphthyl rings enhancing the overlap of the π systems in a slipped-stack, J-aggregate structure. Additionally, the *n*-alkoxy groups can potentially exert a structural ordering effect in spin-cast films to enhance long-range order, π-stacking, and improve orbital overlap, as is seen in substituted perylene diimides.[29]

Thin-Film Microstructure and Electrical Performance. Although there are many factors influencing field-effect mobility (μ_{FE}) in MPc and MNc OTFTs, there is often a strong correlation in μ_{FE} with microscopic molecular ordering or thin-film microsctructure.[12,30] Atomic force microscopy (AFM) images of OBNc films spin-cast from a 2 wt % solution in toluene on OTS-treated SiO_2 substrates are presented in Figure 3. Unannealed OBNc films are nearly featureless and smooth, with a calculated root-mean-square (rms) roughness of 0.3 nm (Figure 3a). Annealing at 120 °C causes large micrometer-sized domains to form with apparent grain boundaries and a rms roughness of 3.4 nm (Figure 3b). The phase images presented in the Supporting Information (Figure S1) further illustrate the change in surface texture associated with the observed domain features in the AFM. The topography and phase data suggest that annealing induces extended crystallization and possibly enhanced long-range ordering throughout the film. This hypothesis is supported by the red-shifted Q-band observed in the UV−vis spectra, as described earlier. Since OBNc molecular crystals form when a solution is evaporated slowly, as observed in the X-ray data (Figure 1), it is possible that annealing the thin films induces ordered molecular stacks as observed by the large domain regions in Figure 3b.

Although the unannealed films do not exhibit evidence of long-range molecular ordering in the topographical data, the current−voltage data still demonstrate characteristic OTFT output and transfer behavior as shown in Figure 4. The hysteresis output ($I_{ds}-V_{ds}$) and transfer ($I_{ds}-V_{gs}$) data for unannealed spin-cast OBNc OTFTs on OTS-treated SiO_2/n^+Si substrates are presented in Figures 4a and 4d. The output data reveals distinct linear and saturation modes of operation (Figure 4a), and the transfer data has sharp turn-on behavior (Figure 4d) with small hysteresis. A μ_{FE} of 0.003 $cm^2\ V^{-1}\ s^{-1}$, V_{th} of −0.68 V, and $I_{on}/I_{off} > 10^5$ were calculated for the unannealed device in Figure 4d.

The same device characterized in Figures 4a and 4d was annealed at 120 °C, which improved the OTFT performance (Figures 4b and 4e). The field-effect mobility increased by over an order of magnitude to 0.059 $cm^2 V^{-1} s^{-1}$, and the I_{on}/I_{off} ratio increased to more than 10^6. The V_{th} increased slightly to −0.91 V, yet the turn-on voltage remained near 0 V. The results for this device are typical for OBNc OTFTs, and the average device characteristics for multiple process rounds of unannealed and annealed OBNc OTFTs are presented in Table 1.

The vacuum-deposited H_2Pc OTFTs used in this study have low performance with large hysteresis in the output (Figure 4c) and transfer (Figure 4f) data. The figures of merit listed in Table 1 are comparable to reported H_2Pc OTFTs[12,19] but still worse than the unannealed OBNc OTFTs. Therefore, despite the smooth AFM topography observed for unannealed OBNc films in Figure 3a, the $I-V$ and spectroscopic data suggest OBNc forms ordered layers near the OTS treated SiO_2. By annealing, the layers likely become more ordered by forming crystalline regions which extend from the interface to the surface. Enhanced ordering for annealed OBNc OTFTs is consistent with the observation of large domains in Figure 3b and the improved transport characteristics.

Ambient Stability. OTFT sensors require air-stable operation characteristics to reduce transient baseline drift.

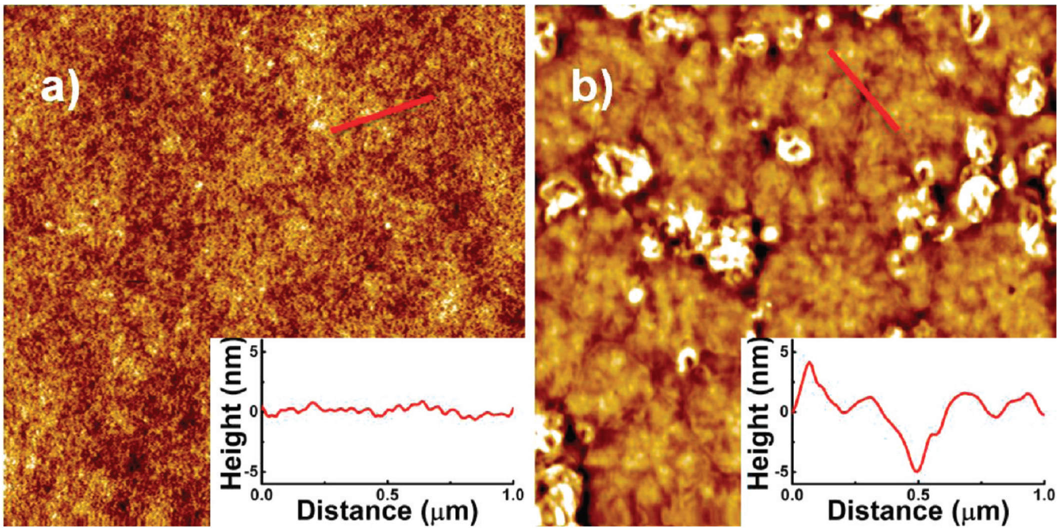

Figure 3. Atomic force microscopy (AFM) images of a 5 μm × 5 μm region of spin-cast OBNc on OTS-treated SiO_2 (a) before annealing and (b) after annealing at 120 °C. The insets show line profiles of a 1 μm segment indicated by the red line in the image. The height scale on the line profiles is held constant to illustrate the flat, featureless surfaces for unannealed OBNc films and the rougher surface with possible grain boundaries for the annealed OBNc films.

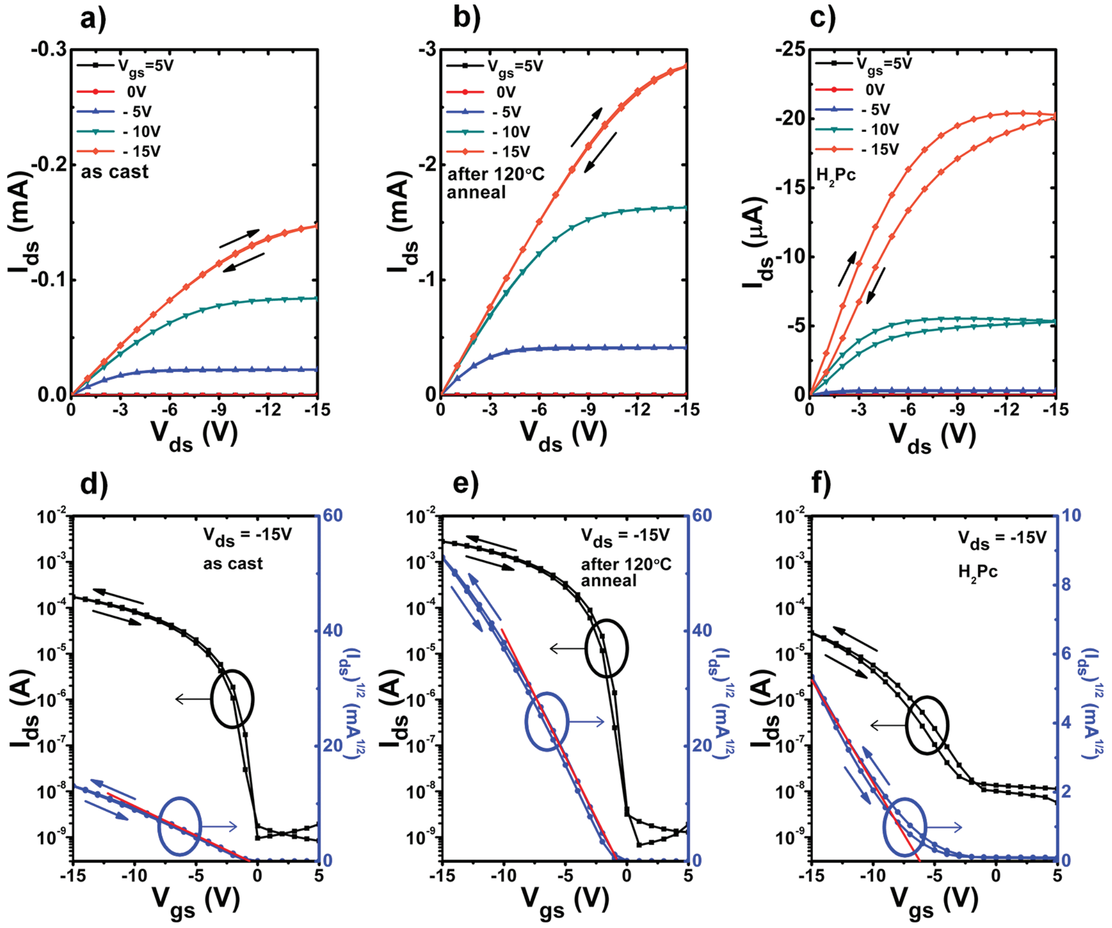

Figure 4. Current−voltage characterization of unannealed and annealed spin-cast OBNc OTFTs and vacuum-deposited H_2Pc OTFTs on OTS-treated substrates. Hysteresis output data for an (a) unannealed OBNc OTFT, (b) annealed OBNc OTFT, and (c) H_2Pc OTFT. Hysteresis transfer data for (d) an unannealed OBNc OTFT, (e) annealed OBNc OTFT, and (f) H_2Pc OTFT. The sweep direction is indicated for the hysteresis measurements. All sweeps were performed using a medium integration time. The red line indicates the line of fit used for μ_{FE} and V_{th} calculation. For each device, the gate oxide capacitance C_i = 34.5 nF cm^{-2}, the channel width $W = 10^5$ μm, and the channel length L = 5 μm.

Table 1. Average Device Characteristics for Multiple Spin-Coated Unannealed and Annealed OBNc OTFTs and Vacuum-Deposited H_2Pc OTFTs[a]

	μ_{FE} ($cm^2\ V^{-1}\ s^{-1}$)	V_{th} (V)	I_{on}/I_{off}	S (V/decade)
as-cast OBNc	0.003 ± 0.0001	-0.58 ± 0.08	$(6.1 \pm 0.8) \times 10^4$	0.49 ± 0.02
annealed OBNc	0.055 ± 0.005	-0.88 ± 0.15	$(1.2 \pm 0.4) \times 10^6$	0.41 ± 0.03
H_2Pc	0.001 ± 0.0002	-6.5 ± 0.21	$(4.7 \pm 2.6) \times 10^3$	2.4 ± 0.1

[a] Parameters for all devices were calculated from the off-to-on transfer sweep.

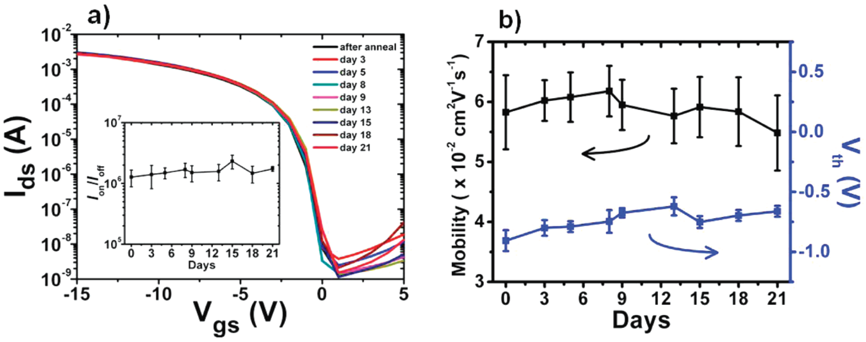

Figure 5. (a) Transfer data for an annealed OBNc OTFT stored in ambient air for 3 weeks. The inset to (a) plots the calculated I_{on}/I_{off} ratio for each transfer curve. (b) μ_{FE} and V_{th} calculated from the transfer data in (a), demonstrating small changes when exposed to ambient air for 3 weeks.

Table 2. Calculated Sensitivities (S), Standard Deviations (σ S), and Enhancement Factors (S_{OBNc}/S_{H2Pc}) of OBNc and H_2Pc OTFT Sensors Monitored at $V_{gs} = V_{ds} = -10$ V[a]

analyte	S (% ppm^{-1}) (OBNc)	σ S (OBNc)	S (% ppm^{-1}) (H_2Pc)	σ S (H_2Pc)	S_{OBNc}/S_{H2Pc}
DMMP	−0.23	0.004	−0.071	0.007	3.3
DMSO	−0.85	0.010	−0.20	0.018	4.2
TMP	−0.17	0.005	−0.079	0.017	2.1
TOL	-3.9×10^{-3}	7×10^{-5}	-8.7×10^{-4}	3×10^{-5}	4.6
DEE	-1.1×10^{-3}	1×10^{-5}	-2.1×10^{-4}	2×10^{-5}	5.1
IPA	-3.1×10^{-3}	1×10^{-5}	-7.9×10^{-4}	5×10^{-5}	3.9
H_2O	-1.0×10^{-3}	7.5×10^{-4}	-8.8×10^{-4}	5×10^{-5}	1.1
MeOH	-7.9×10^{-4}	1×10^{-5}	-3.6×10^{-4}	2×10^{-5}	2.2

[a] Abbreviations: dimethyl methylphosphonate (DMMP), dimethyl sulfoxide (DMSO), trimethyl phosphate (TMP), toluene (TOL), diethyl ether (DEE), isopropanol (IPA), methanol (MeOH).

Significant efforts have been made to isolate the atmospheric species responsible for OTFT performance degradation in ambient atmosphere; however, the results vary for different organic semiconductors.[22,31−33] Pentacene and other acene-derivative OTFT materials are highly susceptible to degradation by O_2 and H_2O,[32−34] whereas polythiophene and MPc OTFTs are more susceptible to degradation in the presence of trace pollutant oxidants such as NO_2 and O_3.[22,31] Having air-stable semiconductor films would eliminate the need for complicated processing and operational techniques used to prevent or refresh air-induced degradation.[35]

To test the air stability of the annealed OBNc OTFTs, the transport properties of annealed OBNc OTFTs were recorded for a 3 week period while the devices were exposed to ambient air (Figure 5a). The transfer data remain nearly unchanged over the 3 week period, and the I_{on}/I_{off} ratio is plotted for each measurement (inset to Figure 5a). Mobility and threshold voltages were also calculated from the transfer data and are plotted in Figure 5b. The mobility is approximately constant within the range of error, and the threshold voltage shifts by less than +0.25 V. These values are much improved over MPc OTFTs, which exhibit V_{th} increases of several volts and I_{on}/I_{off} ratio decreases of nearly an order of magnitude when exposed to air for only 1 day.[21] In addition, the OBNc OTFTs maintain a hysteresis of less than 0.25 V in the transfer data over the 3 week period (Figure S2), which is an order of magnitude improvement compared to reported hysteresis values for high performance soluble phthalocyanines.[24]

One possible explanation for the improved stability of OBNc OTFTs to air is the antioxidant property of the butoxy substituents. The H atoms adjacent to the C−O bond are prone to hydrogen abstraction reactions with free radical oxidants and could serve as hydrogen atom donors to scavenge trace strong ambient oxidants (e.g., ozone and NO_x). Otherwise, degradation of the π-conjugated naphthalocyanine ring system would occur, causing I_{off} and V_{th} to increase. Additionally, the hydrocarbon side chains on OBNc may enhance the hydrophobicity of the surface and hinder H_2O diffusion through the film. Water has been cited as causing hysteresis in OTFTs due to H_2O-induced electron trapping within the semiconductor and at the interface.[36] This mechanism for increased ambient stability is consistent with the sensing data presented below, which demonstrates a 2−5 times increase in sensitivity for OBNc sensors to most analytes with the exception of water. Therefore, the small hysteresis for fresh and aged OBNc devices suggests resistance to atmospheric impurity diffusion in OBNc spin-cast films.

Chemical Vapor Sensing. Despite the resistance to degradation in ambient air, the OBNc OTFTs demonstrate excellent sensitivity to hydrogen bond acceptor analytes. The analytes (listed in Table 2) were chosen to span a wide range of hydrogen bond acceptor strengths. In previous work, similar analytes were used to evaluate the analyte/semiconductor hydrogen bonding properties of vacuum-deposited H_2Pc chemiresistors.[18] Both OBNc and H_2Pc have identical core molecular structures with two hydrogen-bond active N−H groups in the center of the macrocycle. Therefore, the present study analyzed annealed spin-cast OBNc and vacuum-deposited H_2Pc OTFT sensors to compare analyte/semiconductor binding properties based on OTFT device characteristics. The OTFT sensors were monitored by periodic transfer curve (I_{ds}−V_{gs}) measurements, with V_{gs} sweeps from +10 to −10 V. This enables independent determination of the analyte effect on both the field-effect mobility (μ_{FE}) and threshold voltage (V_{th}).

For all analytes, the dosing was performed well below the saturation vapor pressure so as to only perturb the electronic structure of the film instead of inducing morphological changes such as swelling or lattice reorganization, which could significantly change threshold voltages.[37] Therefore, when operating in the accumulation regime ($V_{gs} < V_{th}$), the mobility changes dominate current response ($\Delta I_{ds}/I_{ds0}$). The $\Delta I_{ds}/I_{ds0}$ response for OBNc and H_2Pc sensors at V_{gs} = −10 V is plotted for toluene (TOL), dimethyl sulfoxide (DMSO), and trimethyl phosphate (TMP) in Figure 6. The sensitivity is calculated from the peak to peak response ($R = \Delta I_{ds}/I_{baseline}$) between the beginning and the end of the dose. The sensitivity (S) is a function of concentration (c) and defined as the slope of R plotted against dose concentration; therefore, $S(c) = \partial R/\partial c$. The graphical representation of sensitivity is presented in Figure S6. The OBNc sensors exhibit 2−5 times improved sensitivity for most analytes (Table 2). As shown in Figure S4, the $\Delta\mu_{FE}/\mu_{FE0}$ demonstrates nearly identical sensitivity improvements for OBNc OTFTs relative to H_2Pc OTFTs. The mobility decreases are consistent with increased carrier trap energies and perturbation of electronic structure due to analyte binding.[38−40]

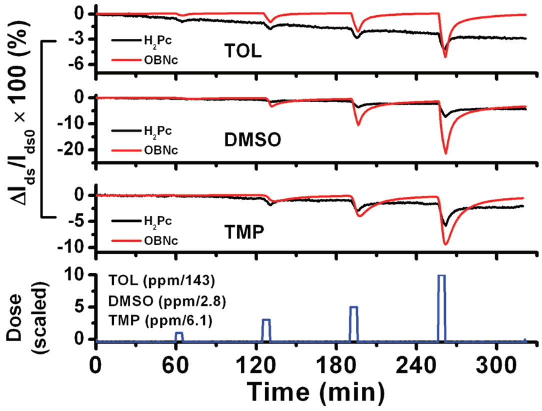

Figure 6. Transient sensing data for vacuum-deposited H_2Pc and spin-cast OBNc OTFTs exposed to 5 min pulses of 143−1430 ppm toluene (TOL), 2.8−28 ppm dimethyl sulfoxide (DMSO), and 6.1−61 ppm trimethyl phosphate (TMP). The drain current (I_{ds}) was recorded for the conditions $V_{ds} = V_{gs}$ = −10 V. All other transient I_{ds} sensing data at V_{gs} = −10 V can be found in the Supporting Information Figure S3.

Both sensors demonstrate 40−1000 times higher sensitivities to strong hydrogen bond acceptor analytes (strong binders) such as DMMP, DMSO, and TMP, relative to the weak hydrogen bond acceptor analytes (weak binders), MeOH, IPA, TOL, DEE, and water (Figure 7). The similarities in sensor response at high V_{gs} suggest that both OBNc and H_2Pc OTFTs are significantly influenced by analyte hydrogen bond affinity, as previously observed for H_2Pc chemiresistors.[18] The improved sensitivity for OBNc could be attributed to the larger intermolecular spacing in the OBNc crystal structure, but no correlation between sensitivity and analyte size was observed. Therefore, the improved sensitivity and larger μ_{FE} decreases for OBNc OTFTs are more consistent with improved analyte binding and/or greater perturbation of the OBNc electronic structure.

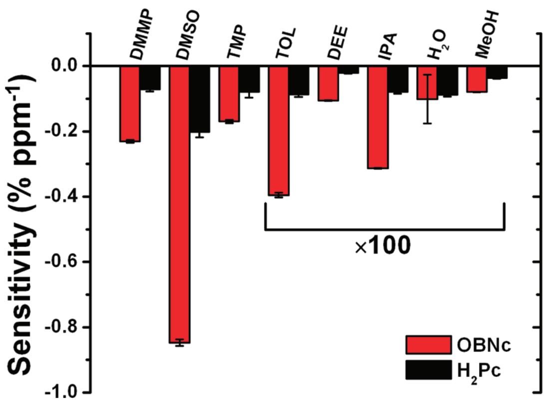

Figure 7. Calculated sensitivities for OBNc and H_2Pc OTFT sensors monitored at V_{gs} = −10 V and V_{ds} = −10 V. The sensitivity is calculated from the peak to peak response ($R = \Delta I_{ds}/I_{baseline}$) between the beginning and the end of the dose, and the sensitivity is the slope of R plotted against dose concentration, c; therefore, $S(c) = \partial R/\partial c$. The error bars represent standard deviations of the sensitivity calculations for three OBNc or H_2Pc sensors.

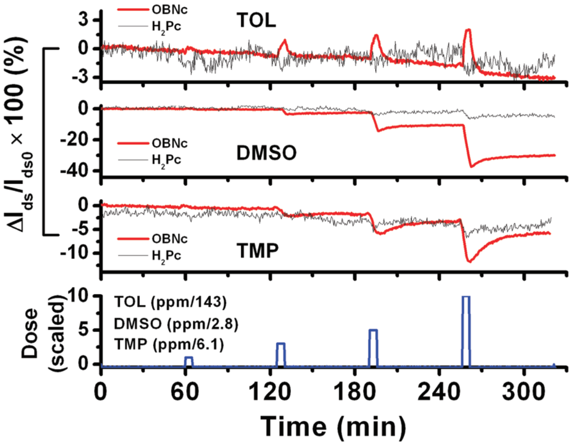

Figure 8. Transient sensing data for vacuum deposited H_2Pc and spin-cast OBNc OTFTs exposed to 5 min pulses of 143−1430 ppm toluene (TOL), 2.8−28 ppm dimethyl sulfoxide (DMSO), and 6.1−61 ppm trimethyl phosphate (TMP). The drain current (I_{ds}) was recorded at V_{ds} = −10 V, V_{gs} = 0 V for OBNc OTFTs and V_{ds} = −10 V, V_{gs} = −6 V for H_2Pc OTFTs. The different V_{gs} accounts for the different V_{th}, so that both sensors are monitored in the OTFT subthreshold regime ($V_{gs} \approx V_{th}$). All other transient I_{ds} sensing data at these gate voltages can be found in the Supporting Information Figure S5.

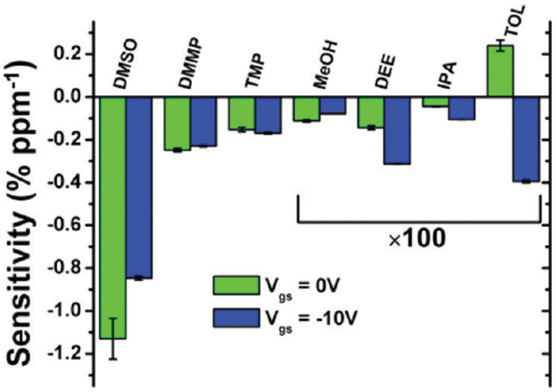

Figure 9. Calculated analyte sensitivities for OBNc OTFTs compared for $V_{gs} = -10$ V and $V_{gs} = 0$ V. Note that although the response at $V_{gs} = 0$ V is reversible for some analytes and irreversible for others, the peak to peak I_{ds} response, was used to calculate sensitivity in all cases. The sensitivity is calculated from the peak to peak response ($R = \Delta I_{ds}/I_{baseline}$) between the beginning and the end of the dose at the specified V_{gs}. The sensitivity is defined as the slope of R plotted against dose concentration, c; therefore, $S(c) = \partial R/\partial c$. The error bars represent standard deviations of the sensitivity calculations for three OBNc sensors.

When the OTFT drain current is monitored in the subthreshold regime ($V_{gs} \approx V_{th}$), OTFT sensors become highly sensitive to V_{th} changes. In the absence of analytes, the V_{th} for OBNc OTFTs are ~7 times smaller than for H_2Pc OTFTs, consistent with less uncompensated charge in OBNc films compared to H_2Pc films. This is reasonable since the H_2Pc vapor deposition temperature is high enough to cause thermal decomposition of organic contaminants, which may introduce radical fragments that form anions in the H_2Pc film, yielding the strongly negative threshold voltage for H_2Pc OTFTs. Therefore, to sense I_{ds} in the subthreshold regime, I_{ds} was monitored at $V_{gs} = -6$ V for H_2Pc OTFTs and $V_{gs} = 0$ V for OBNc OTFTs.

When I_{ds} is monitored at $V_{gs} = 0$ V, OBNc OTFTs exhibit significant differences among the tested analytes, demonstrating selective sensor properties (Figure 8). The DMSO response at $V_{gs} = 0$ V (Figure 8) is larger and irreversible compared to the response at $V_{gs} = -10$ V (Figure 6). The irreversible negative response at $V_{gs} = 0$ V is exclusive for the more polar analytes and consistent with a negative V_{th} shift due to analyte-stabilized negative charge. For some analytes such as TMP, there is a negligible change in V_{th}, and the response at both gate voltages are nearly equal, consistent with the analyte primarily causing a decrease in mobility. The H_2Pc OTFT sensor ($V_{th} \approx -6$ V) does not exhibit significant V_{th} response to any analyte, and $\Delta I_{ds}/I_{ds0}$ is nearly equal when sensing at either $V_{gs} = -6$ V or $V_{gs} = -10$ V. Additionally, the low mobility for H_2Pc makes sensing at V_{gs} near V_{th} difficult due to the small currents, which cause low signal-to-noise ratio as observed in Figure 8.

Enhanced selectivity is demonstrated with OBNc OTFTs in Figure 8 due to bipolar response characteristics when sensing in the subthreshold regime. The calculated sensitivities based on analyte-induced current change for OBNc OTFTs are compared for high V_{gs} and low V_{gs} in Figure 9, and the values are presented in Table 3. An effective metric for selectivity is the relative sensitivity ratio $(S_{10} - S_0)/S_{10}$, where S_{10} is the sensitivity for $V_{gs} = -10$ V and S_0 is the sensitivity for $V_{gs} = 0$ V. This is plotted in Figure 10a for each analyte, where a distinction has been noted for the strong and weak binding analytes. Figure 10a illustrates enhanced selectivity among the strong binders and among the weak binders since distinct ratios are observed within both analyte classes. Although DMSO and MeOH have similar sensitivity ratios, the calculated sensitivity for DMSO is more than 1000 times larger than the sensitivity for MeOH at both high and low V_{gs}. Therefore, the OBNc sensors remain selective between strong and weak binding analytes.

Polar analytes have been noted for causing V_{th} shifts in OTFT sensors due to stabilization of charge within the sensor film.[41] To better understand the analyte properties which cause charge stabilization in OBNc sensors, the sensitivity ratios for strong and weak binding analytes were plotted against the octanol−water partition coefficient in Figures 10b and Figure 10c. A clear correlation with analyte hydrophobicity is observed in both plots, consistent with the analyte solubility in polar/ionic media. The most polar analytes among the strong and weak binders (DMSO and MeOH) cause larger, irreversible responses when OBNc OTFTs are operated at $V_{gs} = 0$ V. Therefore, the data in Figures 10b and Figure 10c suggest that analytes with a ratio less than 0 better stabilize negative charge and cause negative V_{th} shifts. Conversely, nonpolar analytes such as toluene have ratios greater than 0 which is consistent with their inability to stabilize negative charge. Instead, these analytes could cause increases in V_{th} through van der Waals interactions or possibly contact effects.[42] Water is omitted from Figures 9 and 10 due to anomalous transient behavior in which the current reversibly increased during the dose but irreversibly decreased after the dose. Therefore, there could be multiple precursor sites for adsorbed water, which influence V_{th} prior to stabilizing charge in the film.

Table 3. Calculated Sensitivities for OBNc OTFT Sensors Monitored at $V_{gs} = -10$ V (S_{10}) and $V_{gs} = 0$ V (S_0), with Standard Deviations (σ S_{10}, σ S_0) and Relative Sensitivity Ratios $(S_{10}-S_0)/S_{10}$[a]

analyte	S_{10} (% ppm^{-1})	σ S_{10}	S_0 (% ppm^{-1})	σ S_0	$(S_{10} - S_0)/S_{10}$
DMMP	−0.23	0.004	−0.25	0.009	−0.078
DMSO	−0.85	0.010	−1.13	0.10	−0.33
TMP	−0.17	0.005	−0.15	0.01	0.099
TOL	-3.9×10^{-3}	7×10^{-5}	2.4×10^{-3}	2.5×10^{-4}	1.6
DEE	-1.1×10^{-3}	1×10^{-5}	-4.5×10^{-4}	1×10^{-5}	0.57
IPA	-3.1×10^{-3}	1×10^{-5}	-1.4×10^{-3}	9×10^{-5}	0.54
H_2O	-1.0×10^{-3}	7.5×10^{-4}	undef	undef	undef
MeOH	-7.9×10^{-4}	1×10^{-5}	-1.1×10^{-3}	6×10^{-5}	−0.41

[a] The response for water at $V_{gs} = 0$ V increases and decreases during dosing therefore the sensitivity is not well-defined.

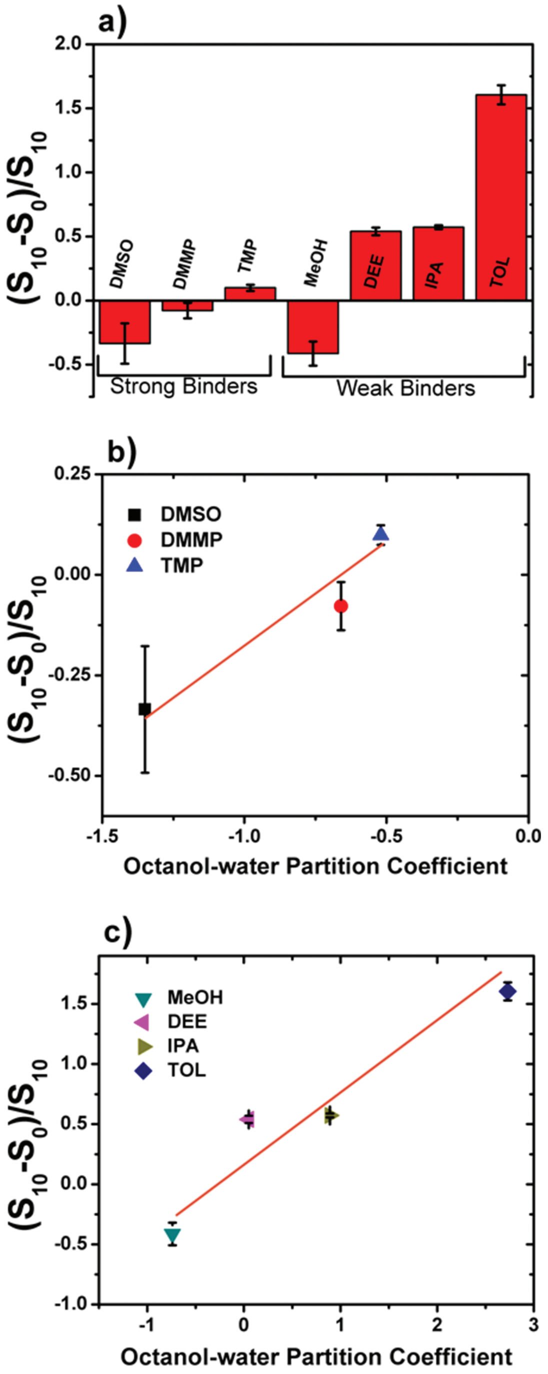

Figure 10. (a) Relative sensitivity ratio $(S_{10} - S_0)/S_{10}$ for OBNc OTFT sensors where S_{10} is the sensitivity for $V_{gs} = -10$ V and S_0 is the sensitivity for $V_{gs} = 0$ V. Relative sensitivity ratio plotted against the octanol–water partition coefficient for (b) the strong binding analytes and (c) the weak binding analytes. Ratios significantly greater than or less than 0 indicate strong influence of the analyte on V_{th}. The trend illustrates how more polar analytes stabilize negative charge. The standard deviations were calculated using the values for $\sigma\ S_{10}$ and $\sigma\ S_0$ and propagating the error for the equation $(S_{10} - S_0)/S_{10}$.

CONCLUSIONS

Air-stable OBNc OTFT chemical sensors demonstrate unique dual response characteristics which yield improved sensitivity and selectivity over more conventional vacuum-deposited H_2Pc OTFTs. The sensor improvements for OBNc are partially attributed to the improved transport properties which exhibit mobilities of 0.06 $cm^2\ V^{-1}\ s^{-1}$, $I_{on}/I_{off} > 10^6$, and low threshold voltages ($|V_{th}| < 1$ V). For most analytes, the OBNc OTFTs demonstrate 2–5 times larger mobility decreases, which are attributed to stronger analyte -induced perturbation of the OBNc electronic structure. The OBNc OTFTs have enhanced selectivity when I_{ds} is monitored in the subthreshold regime due to irreversible threshold voltage shifts. The threshold voltage may increase or decrease depending on the analyte's octanol–water partition coefficient. Therefore, the magnitude and irreversibility of the subthreshold I_{ds} response appears related to the analyte's ability to stabilize negative charge in the OBNc film. H_2Pc OTFTs are not as selective since they only exhibit mobility decreases and are poorer sensors in the subthreshold regime due to the poorer OTFT device performance. Using the OBNc material template, metal–octabutoxynaphthalocyanines are currently being investigated for complementary sensor properties. Utilizing high and low V_{gs} sensing on an octabutoxynaphthalocyanine array could yield highly selective vapor sensors.

ASSOCIATED CONTENT

Ⓢ Supporting Information

Crystallographic information file (CIF) for OBNc, AFM phase data for OBNc, aged OBNc hysteresis current–voltage data, mobility sensing data, current sensing data for other analytes at high and low V_{gs}, and example sensitivity calculation. This material is available free of charge via the Internet at http://pubs.acs.org.

AUTHOR INFORMATION

Corresponding Author

*E-mail: akummel@ucsd.edu (A.C.K.), wtrogler@ucsd.edu (W.C.T.).

Notes

The authors declare no competing financial interest.

ACKNOWLEDGMENTS

Support by AFOSR STTR II Contracts FA9550-10-C-0019 and FA9550-10-C-0011 is gratefully acknowledged along with NSF Grant CHE-0848502. The authors thank Dr. Curtis Moore of the UCSD Small Molecule Crystallography Facility for the structure determination and Erik Kappe for designing the LabVIEW sensing program.

REFERENCES

(1) Arias, A. C.; MacKenzie, J. D.; McCulloch, I.; Rivnay, J.; Salleo, A. *Chem. Rev.* **2010**, *110*, 3–24.

(2) Bouvet, M. *Anal. Bioanal. Chem.* **2006**, *384*, 366–373.

(3) Bouvet, M.; Xiong, H.; Parra, V. *Sens. Actuators, B* **2010**, *145*, 501–506.

(4) Huang, J.; Dawidczyk, T. J.; Jung, B. J.; Sun, J.; Mason, A. F.; Katz, H. E. *J. Mater. Chem.* **2010**, *20*, 2644–2650.

(5) Angione, M. D.; Pilolli, R.; Cotrone, S.; Magliulo, M.; Mallardi, A.; Palazzo, G.; Sabbatini, L.; Fine, D.; Dodabalapur, A.; Cioffi, N.; Torsi, L. *Mater. Today* **2011**, *14*, 424–433.

(6) See, K. C.; Becknell, A.; Miragliotta, J.; Katz, H. E. *Adv. Mater.* **2007**, *19*, 3322.

(7) Huang, J.; Sun, J.; Katz, H. E. *Adv. Mater.* **2008**, *20*, 2567.

(8) Dezieck, A.; Acton, O.; Leong, K.; Oren, E. E.; Ma, H.; Tamerler, C.; Sarikaya, M.; Jen, A. K. Y. *Appl. Phys. Lett.* **2010**, *97* (1), 013307.

(9) Katz, H. E. *Chem. Mater.* **2004**, *16*, 4748–4756.

(10) Chang, J.; Liu, V.; Subramanian, V.; Sivula, K.; Luscombe, C.; Murphy, A.; Liu, J.; Frechet, J. *J. Appl. Phys.* **2006**, *100*, 14506.

(11) Bora, M.; Schut, D.; Baldo, M. A. *Anal. Chem.* **2007**, *79*, 3298–3303.
(12) Bao, Z. N.; Lovinger, A. J.; Dodabalapur, A. *Adv. Mater.* **1997**, *9*, 42.
(13) Dong, S. Q.; Tian, H. K.; Song, D.; Yang, Z. H.; Yan, D. H.; Geng, Y. H.; Wang, F. S. *Chem. Commun.* **2009**, 3086–3088.
(14) Wang, B.; Zuo, X.; Cheng, X. L.; Wu, Y. Q. *Thin Solid Films* **2008**, *517*, 937–942.
(15) Cook, M. J.; Dunn, A. J.; Howe, S. D.; Thomson, A. J.; Harrison, K. J. *J. Chem. Soc., Perkin Trans. 1* **1988**, 2453–2458.
(16) Bohrer, F. I.; Colesniuc, C. N.; Park, J.; Ruidiaz, M. E.; Schuller, I. K.; Kummel, A. C.; Trogler, W. C. *J. Am. Chem. Soc.* **2009**, *131*, 478–485.
(17) Tran, N. L.; Kummel, A. C. *J. Chem. Phys.* **2007**, *127*, 214701.
(18) Bohrer, F. I.; Sharoni, A.; Colesniuc, C.; Park, J.; Schuller, I. K.; Kummel, A. C.; Trogler, W. C. *J. Am. Chem. Soc.* **2007**, *129*, 5640–5646.
(19) Royer, J. E.; Lee, S.; Chen, C.; Ahn, B.; Trogler, W. C.; Kanicki, J.; Kummel, A. C. *Sens. Actuators, B* **2011**, *158*, 333–339.
(20) Shea, P. B.; Kanicki, J.; Cao, Y.; Ono, N. *Appl. Phys. Lett.* **2005**, *87*, 173506.
(21) Yan, X.; Wang, H.; Yan, D. *Thin Solid Films* **2006**, *515*, 2655–2658.
(22) Park, J.; Royer, J. E.; Colesniuc, C. N.; Bohrer, F. I.; Sharoni, A.; Jin, S. H.; Schuller, I. K.; Trogler, W. C.; Kummel, A. C. *J. Appl. Phys.* **2009**, *106*, 034505.
(23) Hirao, A.; Akiyama, T.; Okujima, T.; Yamada, H.; Uno, H.; Sakai, Y.; Aramaki, S.; Ono, N. *Chem. Commun.* **2008**, 4714–4716.
(24) Chaure, N. B.; Cammidge, A. N.; Chambrier, I.; Cook, M. J.; Cain, M. G.; Murphy, C. E.; Pal, C.; Ray, A. K. *Sci. Technol. Adv. Mater.* **2011**, 025001.
(25) Rihter, B. D.; Kenney, M. E.; Ford, W. E.; Rodgers, M. A. J. *J. Am. Chem. Soc.* **1993**, *115*, 8146–8152.
(26) Park, J.; Yang, R. D.; Colesniuc, C. N.; Sharoni, A.; Jin, S.; Schuller, I. K.; Trogler, W. C.; Kummel, A. C. *Appl. Phys. Lett.* **2008**, *92*, 193311.
(27) Tai, S.; Hayashi, N.; Katayose, M. *Prog. Org. Coat.* **1994**, *24*, 323–339.
(28) Katayose, M.; Tai, S.; Kamijima, K.; Hagiwara, H.; Hayashi, N. *J. Chem. Soc., Perkin Trans. 2* **1992**, 403–409.
(29) Xue, C.; Jin, S. *Chem. Mater.* **2011**, *23*, 2689–2692.
(30) Li, L. Q.; Tang, Q. X.; Li, H. X.; Hu, W. P. *J. Phys. Chem. B* **2008**, *112*, 10405–10410.
(31) Chabinyc, M. L.; Street, R. A.; Northrup, J. E. *Appl. Phys. Lett.* **2007**, *90*, 123508.
(32) Northrup, J. E.; Chabinyc, M. L. *Phys. Rev. B* **2003**, *68*, 041202.
(33) Maliakal, A.; Raghavachari, K.; Katz, H.; Chandross, E.; Siegrist, T. *Chem. Mater.* **2004**, *16*, 4980–4986.
(34) Park, S. K.; Mourey, D. A.; Han, J.-I.; Anthony, J. E.; Jackson, T. N. *Org. Electron.* **2009**, *10*, 486–490.
(35) Hyung, G. W.; Park, J.; Kim, J. H.; Koo, J. R.; Kim, Y. K. *Solid-State Electron.* **2010**, *54*, 439–442.
(36) Gu, G.; Kane, M. G. *Appl. Phys. Lett.* **2008**, *92*, 3.
(37) Street, R. A.; Chabinyc, M. L.; Endicott, F. *Phys. Rev. B* **2007**, *76*, 045208.
(38) Yang, R. D.; Gredig, T.; Colesniuc, C. N.; Park, J.; Schuller, I. K.; Trogler, W. C.; Kummel, A. C. *Appl. Phys. Lett.* **2007**, *90*, 263506.
(39) Duarte, D.; Sharma, D.; Cobb, B.; Dodabalapur, A. *Appl. Phys. Lett.* **2011**, *98*, 133302.
(40) Yang, R. D.; Park, J.; Colesniuc, C. N.; Schuller, I. K.; Royer, J. E.; Trogler, W. C.; Kummel, A. C. *J. Chem. Phys.* **2009**, *130*, 164703.
(41) Someya, T.; Dodabalapur, A.; Huang, J.; See, K. C.; Katz, H. E. *Adv. Mater.* **2010**, *22*, 3799–3811.
(42) Torsi, L.; Marinelli, F.; Angione, M. D.; Dell'Aquila, A.; Cioffi, N.; De Giglio, E.; Sabbatini, L. *Org. Electron.* **2009**, *10*, 233–239.